Particle trapped at the isotropic-nematic liquid crystal interface: Elastocapillary phenomena and drag forces

J.-C Loudet, A Choudhury, M Qiu, J Feng

Particle trapped at the isotropic-nematic liquid crystal interface: Elastocapillary phenomena and drag forces

J.-C. Loudet[a,1], A. Choudhury[b,c,2], M. Qiu[d], and J.J. Feng[c,e]

[a] *Université de Bordeaux, CNRS, Centre de Recherche Paul Pascal (UMR 5031), 33600 Pessac, France*

[b] *Department of Mechanical and Aerospace Engineering, Indian Institute of Technology Hyderabad, India*

[c] *University of British Columbia, Department of Mathematics, Vancouver, BC, V6T 1Z2, Canada*

[d] *Laboratoire de Physique, École Normale Supérieure, 75005 Paris, France*

[e] *University of British Columbia, Department of Chemical and Biological Engineering, Vancouver, BC, V6T 1Z3, Canada*

Abstract

We present numerical simulations of a particle trapped at the isotropic-nematic liquid crystal (Iso-N) interface. We use our recent model, based on a phase-field approach (see Qiu *et al.*, Phys. Rev. E, **103**, 022706 (2021)), to couple the capillary forces acting on the interface with the elastic stresses in the nematic phase along with topological defects. A range of floating configurations are first investigated as a function of the contact angle and various anchoring conditions at the fluid interface. The results show that the response of the system is driven by the existence of an anchoring conflict at the contact line. Substantial particle displacements and/or interfacial deformations may occur in this case even for moderate anchoring strengths. These findings highlight the coupling between elastic and capillary forces. In a second part, we compute drag forces exerted on a particle that moves along the Iso-N interface for several contact angles and a moderate Ericksen number. Because

[1]Email: `jean-christophe.loudet@u-bordeaux.fr`

[2]Current address: Université de Paris-Saclay, laboratoire FAST (UMR 7608), 91405, Orsay, France

of the coupling between the velocity and order parameter fields, topological defects are swept downstream of the particle by the flow and sometimes 'escape' from the particle or merge with the interface. We also find linear force-velocity laws, with drag forces at the Iso-N interface being slightly greater than their isotropic counterparts due to director distortions. We discuss these results in light of past studies on the behavior of particles being dragged in the bulk of a liquid crystal matrix.

Keywords: Two-phase flows, particle/fluid flow, phase-field simulations, liquid crystals, elastic distortions, topological defects, interfacial deformations, drag force, elastocapillary phenomena.

1 Introduction

Colloidal dispersions in *bulk* liquid crystal (LC) phases, also known as 'LC colloids' [1], and colloidal particles attached to (isotropic) fluid interfaces [2] are both very rich and versatile systems on their own in soft matter science. They have been extensively investigated, but in a rather independent way so far. Yet, from a self-assembly perspective, both systems share quite a few similarities although the underlying driving physical mechanisms differ greatly. In both cases, the particles may undergo either attractive or repulsive interactions which originate from the deformations of the fluid matrix they are embedded in. In LC colloids, the so-called elastic interactions result from elastic distortions of the LC matrix [1, 3, 4, 5, 6, 7, 8, 9, 10], whereas it is the overlap of interfacial deformations that is responsible for capillary interactions occurring between floating particles [2, 11, 12, 13, 14, 15, 16]. Both elastic and capillary interactions can be long-ranged, anisotropic in nature (e.g., of dipolar or quadrupolar symmetry), and feature energies that greatly exceed the thermal energy k_BT. In both cases, a myriad of colloidal structures, either ordered or disordered, have been discovered depending on numerous factors such as the particle size and shape, surface chemistry (e.g., Janus particles), and confinement (see reviews e.g., [1, 2, 9, 15, 16]).

However, so far only a handful of studies have attempted to bridge the gap between

these two lines of research by studying the behavior of colloids trapped at liquid crystal interfaces. Such systems represent a new kind of soft material whose properties are expected to be governed mainly by the interplay of capillary and elastic phenomena. On the experimental side, a few studies were dedicated to pattern formation, mostly in confined geometries with varying anchoring conditions. For instance, two-dimensional (2D) crystal-like structures and chain-like aggregates were observed at the air-nematic LC (NLC) [17, 18, 19, 20, 21] and water-NLC interfaces [22, 23]. Estimates of pair interaction potentials were derived for both spherical [17, 20] and nonspherical particles [24]. At the single particle level, Jeridi *et al.* [25, 26] reported capillary-induced giant elastic dipoles in thin nematic wetting films, whereas the influence of interfacial curvature was addressed by Gharbi *et al.* [27] by placing particles on NLC shells. More dynamical aspects such as the Brownian diffusion of micro- and nano-particles at the nematic-aqueous phase interface were first investigated by Abras *et al.* [28], whereas the vibrational phonon modes of 2D crystalline packings of particles at the air-NLC interface were discussed by Wei *et al.* [29].

Despite the above discoveries, there is a lack of theoretical understanding of the observed phenomena. Only a few modelling studies have appeared on the subject. Tasinkevych & Andrienko performed the first numerical simulations dealing with particles trapped at an isotropic-nematic (Iso-N) interface in both 2D [30] and 3D [31]. However, they considered a peculiar situation where the interface separates the same mesogenic material in two phases coexisting under the same condition. No interfacial forces nor contact line were taken into account in their analysis. Nevertheless, pair interaction potentials exhibited a rather complex behavior due, in part, to the creation, annihilation and interaction of topological defects in the vicinity of the particles.

Oettel *et al.* [32] considered a more complete physical picture and provided approximate analytical calculations for interacting colloids attached to a nematic free surface. The primary goal was to rationalize the early observations of Smalyukh *et al.* [17], where hexagonal lattices of glycerol droplets were initially thought to result from a competition between an elastic repulsion and a capillary attraction. However, the theoretical analysis of Oettel *et al.* [32] showed that such a competition is unlikely, at least within

the model assumptions and the experimental conditions in [17]. Till today, this remains an open question, and we are not aware of any other detailed theoretical or numerical investigations dealing with these issues.

A possible reason for this is that the modelling of particles adsorbed at LC interfaces is a challenging task. The main difficulty arises from the presence of the interface which couples capillary and elastic phenomena. Indeed, elastic distortions, topological defects, the anchoring of LC molecules on a potentially moving and deformed fluid interface, the contact line dynamics and the particles' motion are all intertwined here. The combination of these phenomena makes these systems very rich but complicates enormously their theoretical treatment.

Recently, our group developed a model that may shed new light on the above problems. The model, based on a phase-field (PF) method, was originally designed to describe elastocapillary flows of LCs [33]. In the present work, we use this model in numerical simulations to explore both the static and the dynamic behaviors of particles trapped at LC interfaces. In view of the dearth of theoretical and numerical studies in the literature, we will focus on 'basic' scientific questions at the single particle level. For instance, how do the LC elasticity and topological defects influence the partial wetting configuration of a particle adsorbed at a LC interface? How do capillarity and elasticity interact? How does interfacial deformation depend on the two factors? What is the drag force exerted on a particle straddling a LC interface? Answers to these questions will form the basis for studying more complex situations involving, e.g., a collection of particles (interactions), confined geometries (thin films), and curved interfaces.

The paper is organized as follows. The model is presented in Sec. 2. It is numerically solved with a finite element method in a 2D planar geometry. In Sec. 3, we first consider the equilibrium configuration of a partially wetting particle on the Iso-N interface, subject to different contact angles and anchoring conditions (Sec. 3.1). Then we study the drag forces for a range of particle positions across the interface (Sec. 3.2). Our results show that wetting configurations are primarily influenced by the existence of an anchoring conflict at the contact line (CL). Sizeable particle displacement and/or interfacial distortions may

occur in this case even for moderate anchoring strengths. The drag force computations reveal linear force-velocity laws. The defect escapes from the particle and merges with the interface in certain circumstances. Furthermore, the drag coefficient at the Iso-N interface is almost always greater than its isotropic counterpart thanks to the coupling between the flow and the order parameter fields. We discuss our results within the framework of existing theories before concluding the paper in Sec. 4.

2 Theoretical model and numerical method

As aforementioned, we have adapted the recent model developed by Qiu *et al.* [33, 34] to describe the behavior of a colloidal particle trapped at the Iso-N fluid interface. The model of Qiu *et al.* [33] uses a phase-field (PF) method to account for elastocapillary flows occurring at the Iso-N interface. It has two key features: (i) A tensor order parameter $\mathbb{Q}$ that provides a consistent description of the molecular and distortional elasticity of the N phase, including topological defects, and (ii) a PF formalism that accurately represents the Iso-N interfacial tension and the nematic anchoring stress by approximating a sharp-interface limit. Combining this with the equations of motion of the fluids, we obtain a model capable of describing the phenomena resulting from the coupling between capillarity and elasticity. All the details and validation examples of this model can be found in [33, 34]. In the following, we only give a brief account of the main ingredients. A notable difference between the present work and that of [33, 34] is the presence of a contact line where the three phases isotropic (Iso), nematic (N), and solid (S) meet. PF-based models can naturally handle the contact line dynamics thanks to intrinsic diffusive processes [35, 36, 37, 38, 39]. Unless otherwise stated, parameter values for the model described in this section are listed in appendix A.

2.1 Free energies

The total free energy of the fluid system consists of the bulk elastic energy of the N phase, f_b , the mixing energy of the Iso-N interface, f_m , and the anchoring energy on the Iso-N

interface, f_a. Note that throughout this work, we assume an infinitely strong anchoring condition of the nematic mesogens on the solid particle and, consequently, the anchoring energy at the nematic-solid interface does not appear. f_b is standard from the nematic order theory [40, 41] and can be described phenomenologically as [42]

$$f_b = \frac{A}{2}Q_{ij}Q_{ij} + \frac{B}{3}Q_{ij}Q_{jk}Q_{ki} + \frac{C}{4}(Q_{ij}Q_{ij})^2 + \frac{L_1}{2}(\partial_i Q_{jk})(\partial_i Q_{jk})\,. \tag{1}$$

Here, A, B, C are material property coefficients ($A, B < 0$, $C > 0$), and L_1 is the bulk elastic constant. As in [33], it is useful to define a scalar order parameter: $q = \sqrt{3/2}\|\mathbb{Q}\|_F = \left(\frac{3}{2}\mathbb{Q} : \mathbb{Q}^\intercal\right)^{1/2}$, where $\|\cdot\|_F$ is the Frobenius norm.

The mixing energy is standard from the PF model and may be written as [43, 44]

$$f_m = \frac{\lambda}{2}\left|\boldsymbol{\nabla}\phi\right|^2 + \frac{\lambda}{4\epsilon^2}\left(\phi^2 - 1\right)^2\,, \tag{2}$$

where ϕ is the PF variable that marks the different fluids. $\phi = -1$ denotes the nematic LC and $\phi = 1$ denotes the isotropic phase. These two fluids mix in a thin diffuse interfacial region in which ϕ and all other variables transition smoothly. The Iso-N interface may be defined by the contour level $\phi = 0$. In Eq. (2), λ is the (constant) mixing energy density with the dimension of force, and ϵ is the (constant) capillary width governing the thickness of the diffuse interface. In the sharp-interface limit, the mixing energy gives rise to an isotropic surface tension given by $\sigma = 2\sqrt{2}\lambda/3\epsilon$ [43, 44].

To describe the finite-strength anchoring of LC molecules at the Iso-N interface, we employ the following diffuse-interface variant of the Rapini-Papoular anchoring energy density [33]

$$f_a = \frac{W}{2}|\boldsymbol{\nabla}\phi|^4 \left\|\mathbb{Q} - q_e\left(\hat{\boldsymbol{e}}\hat{\boldsymbol{e}} - \frac{1}{3}\mathbb{I}\right)\right\|_F^2\,, \tag{3}$$

where W is the (constant) anchoring strength, which can be viewed as an anisotropic surface tension [40], and $\hat{\boldsymbol{e}}$ is a unit vector along the easy direction on the Iso-N interface. Both homeotropic and planar anchoring conditions are considered for $\hat{\boldsymbol{e}}$ with appropriate expressions of f_a in each case (see [33] for details). In Eq. (3), q_e is the equilibrium scalar order parameter under the uniaxial assumption ($q_e = 0.81$ with our parameters, see appendix A). Note that in Eq. (3), W has the dimension of energy×length. In the

sharp interface limit, it can be related to the usual anchoring strength, W_s (unit: J/m^2), via $W = \frac{35}{8\sqrt{2}} W_s \epsilon^3$ as explained in Qiu *et al.* [33].

Hence, the total free energy of the fluid system in a domain Ω is given by

$$F = \int_\Omega f(\phi, \mathbb{Q}, \boldsymbol{\nabla}\phi, \boldsymbol{\nabla}\mathbb{Q})\, dV = \int_\Omega \left(f_m + \frac{1-\phi}{2} f_b + f_a \right)\, dV\,. \tag{4}$$

The factor $(1-\phi)/2$ gives the concentration of the N phase.

2.2 Governing equations

The governing equations include evolution equations for ϕ and $\mathbb{Q}$, and equations of motion for the fluids and the solid particle.

Evolution equation for ϕ. The classical Cahn-Hilliard (CH) equation describes the evolution of ϕ [43, 44]

$$\frac{\partial \phi}{\partial t} + \mathbf{v} \cdot \boldsymbol{\nabla}\phi = \boldsymbol{\nabla} \cdot (\gamma \boldsymbol{\nabla}\mu)\,, \tag{5}$$

where $\mathbf{v}$ is the fluid velocity and γ the mobility constant. $\mu = \delta F_m / \delta\phi$ is the chemical potential which, in our model, is defined only through the mixing energy, $F_m = \int_\Omega f_m\, dV$, i.e. without the contribution from the bulk elastic and anchoring energies. Consequently, the CH diffusion is decoupled from that of $\mathbb{Q}$ [33]. Such an approximation holds in the so-called sharp-interface limit and has been adopted in previous works [44, 45].

Evolution equation for $\mathbb{Q}$. We choose the Beris-Edwards (BE) formalism to describe the nematic hydrodynamics [46]. Within our PF formulation, the evolution equation for $\mathbb{Q}$ in the LC bulk has the same general structure as in the original BE theory [47]

$$\frac{\partial \mathbb{Q}}{\partial t} + \mathbf{v} \cdot \boldsymbol{\nabla}\mathbb{Q} = \mathbb{S} + \Gamma \mathbb{H}\,, \tag{6}$$

where Γ is the (constant) collective rotational diffusion coefficient of the N phase. $\mathbb{H}(\phi, \mathbb{Q}, \boldsymbol{\nabla}\phi, \boldsymbol{\nabla}\mathbb{Q})$ is the molecular field tensor, whereas $\mathbb{S}(\boldsymbol{\nabla}\mathbf{v}, \mathbb{Q})$ is the corotation tensor. Both tensors have been modified in our PF method to take into account the anchoring conditions (either homeotropic or planar) at the Iso-N interface. The resulting lengthy expressions are omitted here but can be found in [33].

Equations of motion for the fluids. Assuming incompressible fluids, we adopt the continuity and Navier-Stokes (NS) equations for the pressure (p) and velocity ($\mathbf{v}$) fields in both phases:

$$\boldsymbol{\nabla}\cdot\mathbf{v} = 0\,, \tag{7}$$

$$\rho(\phi)\left(\frac{\partial\mathbf{v}}{\partial t}+\mathbf{v}\cdot\boldsymbol{\nabla}\mathbf{v}\right) = -\boldsymbol{\nabla}p+\boldsymbol{\nabla}\cdot\mathbb{T}+\mu\boldsymbol{\nabla}\phi\,, \tag{8}$$

where the last body force term in Eq. (8) ($\mu\boldsymbol{\nabla}\phi$) is the diffuse-interface equivalent of the interfacial tension [43, 45]. $\rho(\phi)$ is the density of the two-phase system given by: $\rho(\phi) = \frac{1+\phi}{2}\rho_i + \frac{1-\phi}{2}\rho_n$, where the subscript i (resp., n) refers to the isotropic (resp., nematic) phase. The total stress tensor $\mathbb{T}$ can be written in the following form:

$$\mathbb{T} = -p\mathbb{I}+(1+\phi)\eta_i\mathbb{D}+(1-\phi)\eta_n\mathbb{D}+\mathbb{T}_n\,, \tag{9}$$

where $\mathbb{D} = \left[(\boldsymbol{\nabla}\mathbf{v})^\intercal+\boldsymbol{\nabla}\mathbf{v}\right]/2$ is the rate of deformation tensor. The second term is the viscous stress from the isotropic phase while the third term is a viscous stress of the nematic phase with a constant *effective* viscosity η_n, i.e. independent of the molecular orientation [46, 47]. The last term ($\mathbb{T}_n$) in Eq. (9) is the nematic stress tensor, which has been generalized from the bulk BE theory to take into account the anchoring constraints on the moving Iso-N interface [33]. Note that $\mathbb{T}_n$ intrinsically contains effective anisotropic viscosities [47].

Boundary conditions. For the continuity and NS equations, classical no-slip boundary conditions for $\mathbf{v}$ are imposed on all bounding walls and the particle, unless otherwise stated. On the outer boundaries, we need two BCs for the fourth-order CH equation. First, one often requires that there be no diffusive flux across all boundaries ($\partial\Omega$): $\hat{\mathbf{m}}\cdot\boldsymbol{\nabla}\mu|_{\partial\Omega} = 0$, where $\hat{\mathbf{m}}$ is the outward unit normal vector to a given boundary. Next, we enforce the equilibrium value of the contact angle, θ, at the three-phase contact line on the particle via the geometric boundary condition: $\boldsymbol{\nabla}\phi\cdot\hat{\mathbf{m}} = |\boldsymbol{\nabla}\phi|\cos\theta$, on $\partial\Omega_p$ [Fig. 1(a)]. We also impose a 90°-contact angle on $\partial\Omega_w$ (left side) [Fig. 1(a)], meaning that the interface is flat there but it is free to move up or down.

Concerning the order parameter $\mathbb{Q}$, we consider the following three types of BCs. (i) On all bounding walls, we apply a homogeneous Neumann BC: $\hat{\mathbf{m}}\cdot\boldsymbol{\nabla}\mathbb{Q}|_{\partial\Omega_w} = 0$.

(ii) For simplicity, a Dirichlet BC is used on the particle surface: $\mathbb{Q}|_{\partial\Omega_p} = \mathbb{Q}_D$, where $\mathbb{Q}_D$ corresponds to a uniaxial configuration perpendicular to the particle contour, i.e. homeotropic anchoring, at equilibrium order (q_e). (iii) On the symmetry axis $\partial\Omega_S$, we impose the mixed BC [33]: $\hat{\mathbf{m}} \cdot \boldsymbol{\nabla} (Q_{ii})|_{\partial\Omega_S} = 0$, $Q_{ij}|_{\partial\Omega_S} = 0$ $(i \neq j)$, where ii does not imply the Einstein summation. Finally recall that, at the Iso-N interface, the anchoring conditions are already accounted for in the expressions of $\mathbb{H}$ [Eq. (6)] and $\mathbb{T}$ [Eq. (9)].

Equations of motion of the particle. In some cases, the particle attached to the Iso-N interface is allowed to move in the y-direction (Fig. 1). Its translational velocity (U_y) is governed by Newton's equation of motion written here in the absence of gravity (see Sec. 2.3): $M\dot{U}_y = F_y$, with the initial condition $U_y|_{t=0} = 0$, the dot meaning differentiation with respect to time. M is the particle mass and F_y is the total force exerted on the particle along the y-direction. F_y consists of viscous, elastic, and capillary forces and may be written as

$$F_y = \hat{\mathbf{y}} \cdot \oint_{\partial\Omega_p} (\mathbb{T} + \mathbb{T}_c) \cdot \hat{\mathbf{m}} \, ds \, , \tag{10}$$

where $\hat{\mathbf{y}}$ is the unit normal vector along the y-axis and $\mathbb{T}$ is the stress tensor defined in Eq. (9). $\mathbb{T}_c$ is the capillary stress tensor and can be derived using a variational procedure [44]

$$\mathbb{T}_c = f_{\text{mix}} \, \mathbb{I} - \lambda \boldsymbol{\nabla}\phi\boldsymbol{\nabla}\phi \, , \tag{11}$$

with f_{mix} given by Eq. (2). Once U_y has been determined, the particle's vertical position (y_p) can be updated by solving: $\dot{y}_p = U_y$.

2.3 Geometry and parameters

In this section, we specify the parameters and the two geometries employed in our 2D simulations (Fig. 1). The first one, referred to as problem A hereafter, deals with the equilibrium configuration of a partially wetting particle trapped at the Iso-N interface, whereas the second one, referred to as problem B, is dedicated to the computation of drag forces exerted on the particle straddling the Iso-N interface.

Fig. 1(a,b) specifies the geometry for Problem A. A solid particle of radius R is trapped at the interface between a Newtonian isotropic fluid and a nematic LC. Both fluids have

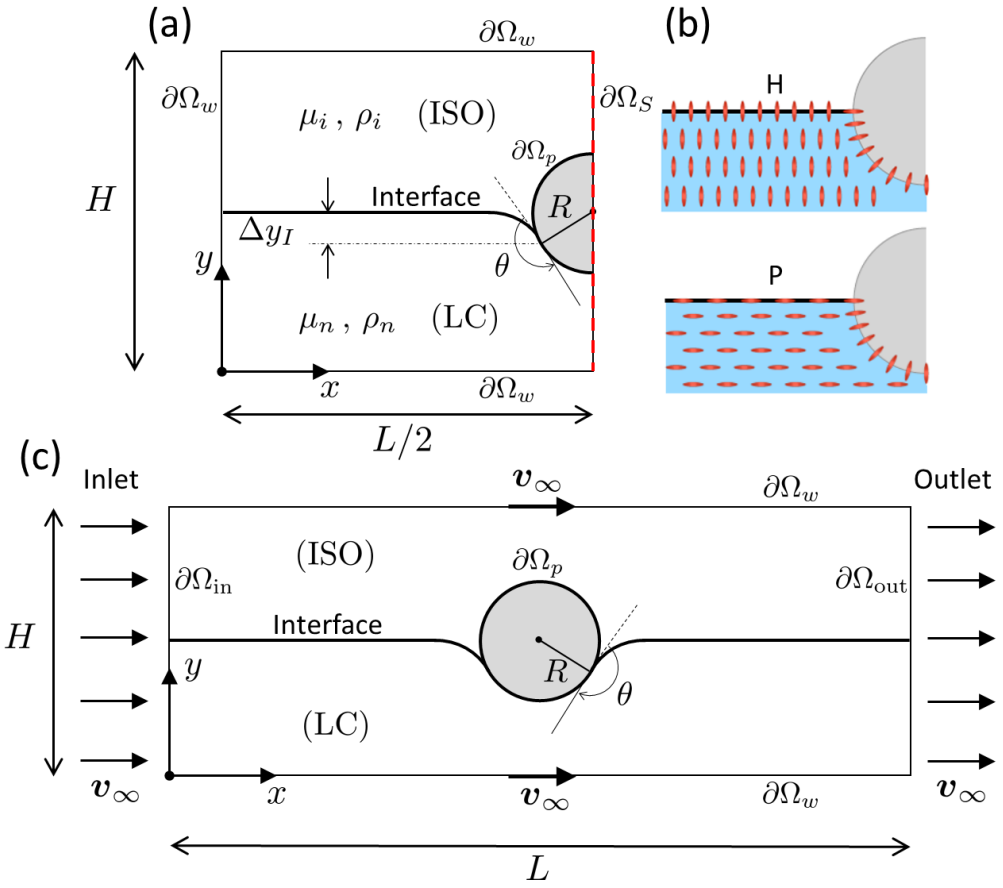

Figure 1: **(a)** Sketch of the simulation domain for Problem A. Box size: $(H, L) = (8R, 10R)$. Symbols: θ: contact angle, Δy_I: interfacial deformation (see text for other symbols definitions). **(b)** Initial bulk and anchoring conditions for the order parameter $\mathbb{Q}$. The small ellipsoids symbolize the LC molecules (not to scale). In all cases, a homeotropic (H) anchoring condition is prescribed at the particle surface, whereas either a homeotropic or planar (P) anchoring is enforced at the Iso-N interface. These two situations are denoted H and P configurations, respectively. **(c)** Geometry for the computation of the two-phase flow drag force exerted on a particle confined at the Iso-N interface between two plane walls (Problem B). Box size: $(H, L) = (20R, 30R)$.

a matched density and the whole system is confined in a box of length $L = 10R$ and height $H = 8R$. However, because of symmetry, we only need to simulate half of the domain. Fig. 1(b) depicts the prescribed anchoring conditions at the Iso-N interface and the particle surface. Both homeotropic (H) and planar (P) anchoring of variable strength W [see Eq. (3)] will be considered on the Iso-N interface, while only an infinitely strong, or rigid, homeotropic anchoring is set on the particle surface (cf. "Boundary conditions" in Sec. 2.2). These two situations will be denoted hereafter as the H and P configurations, respectively. For the initial condition, in the former (resp., the latter) case, we require the far-field LC molecules to be oriented along the vertical (resp., horizontal) direction [Fig. 1(b)] with an equilibrium scalar order parameter q_e (cf. appendix A). Two other configurations, namely a planar anchoring on the particle surface combined with either a planar or homeotropic anchoring at the interface, have been computed as well. However, preliminary results indicate that no new qualitative insights emerge from such configurations, and therefore, we have decided not to include such setups in the present work.

The particle's center of mass is either fixed or allowed to move vertically. The contact angle on the particle surface [Fig. 1(a)] is equal to the equilibrium contact angle θ. The Iso-N interface is initially flat and kept horizontal at the left and right bounding walls of the domain in the course of simulations. However, due to the interplay of elastic distortions, surface tension and anchoring, the interface is likely to be deformed and may be displaced from its initial position as we will see below. Furthermore, since we are typically simulating the behavior of a micrometer-sized particle floating at the Iso-N interface (appendix A), the interfacial deformations arising from the particle's buoyant weight are negligible. Indeed, the Bond number $Bo \simeq 10^{-8}$ for typical parameter values (see e.g. [11]).

Problem B concerns the drag on a circular particle straddling the Iso-N interface [Fig. 1(c)]. We use the same setup as in our previous work with isotropic fluid interfaces [48], except that the bottom fluid is now replaced with the nematic LC. Instead of moving the particle horizontally parallel to the interface, we use a reference frame attached to the

particle so that far from it, both liquids flow with a constant velocity v_∞ in the direction of the x-axis. In this case, the upper and lower bounding plane walls also move with the same velocity v_∞ from left to right in their own planes. Depending on the contact angle, the interface may be deformed near the particle, but it is kept horizontal at the inlet and outlet in all cases.

As aforementioned, our simulations are run with the base parameters listed in appendix A. When presenting the results, we use dimensionless variables marked by an asterisk. Of particular importance is the dimensionless anchoring energy defined by $w^* = W_s/\sigma$. For $w^* \ll 1$, the surface tension dominates anchoring effects and controls the shape of the interface by minimizing distortions. Conversely, interfacial deformations are expected for $w^* \gtrsim 1$, as reported with, e.g., nematic drops immersed in an isotropic fluid [49], or the reverse [50]. Below, we will use w^* as a measure of the anchoring strength. Another important dimensionless quantity is the Ericksen number Er, which is relevant to Problem B. Er is defined as the ratio of viscous to elastic forces [40, 41]: $\mathrm{Er} = \gamma_1 v_\infty R/K$, where $\gamma_1 = 1/\Gamma$ is the nematic rotational viscosity and $K = q_e^2 L_1$ the elastic constant (appendix A). $\mathrm{Er} \ll 1$ (resp., $\mathrm{Er} \gg 1$) implies that the fluid flow has a negligible (resp., dominant) influence on the elastic distortions of the nematic texture.

2.4 Numerical method

The fluid equations, and their associated boundary conditions, together with the particle's equations of motion, are solved numerically until steady state with the finite element computational software COMSOL Multiphysics® [51]. Details of the numerical approximation can be found in [33] and will not be repeated here. Whenever appropriate, we employ the built-in moving mesh module of COMSOL based on an Arbitrary Lagrangian-Eulerian (ALE) scheme to follow and resolve the particle's vertical motion. The amplitude of this motion is always moderate, i.e. typically $\lesssim 0.5R$, and does not incur any remeshing event. As in Qiu *et al.* [33], we design nonuniform triangular meshes fitted with subdomains whose mesh size is adjusted to ensure a sufficient resolution of both the fluid interface [38, 39, 44, 45] and the topological defects as they move around. To appropriately

resolve the defect core, we use a mesh size $h \leqslant 0.75\, l_{\mathrm{nc}}$, where l_{nc} is the nematic coherence length. Outside of the subdomains, the mesh size is much coarser to save computational time.

3 Results and discussion

3.1 Problem A: floating particle

In problem A, we study how the interplay of surface tension, anchoring conditions and nematic elasticity affects the partial wetting configuration of a solid particle trapped at the Iso-N interface. We will first consider a simple situation with a fixed particle to explore the qualitative physical trends, mainly as a function of the anchoring type (H or P configuration) and strength. In a second step, we shall allow the particle to move vertically. Contact angles will range from 45° to 135°.

3.1.1 Fixed particle

We begin with an immobile particle whose center of mass lies in the middle of the box $[(x_p, y_p) = (L/2, H/2)]$ and the contact angle is set to 90° on the particle surface. As explained in Sec. 2.3, the Iso-N interface is initially flat. We examine the influence of the anchoring strength at this interface for both the H and P configurations and we recall that a strong homeotropic anchoring is prescribed at the particle surface (Sec. 2.3). Thus, an anchoring conflict arises in the H configuration at the CL on the particle surface, whereas such a conflict is absent in the P situation [Fig. 1(b)].

Figure 2 depicts the interfacial deformation and the Q-field in the nematic phase for several w^* values. In the H case, the Iso-N interface remains mostly flat for low values of w^* (< 1) and, because of the rigid anchoring imposed on the particle, substantial $\mathbb{Q}$-field distortions occur and extend away from the particle. In this case, the anchoring conflict at the CL is smoothed out and there are no topological defects. Equivalently, we may speak of a large anchoring extrapolation length. However, as we increase w^* (> 1), the elastic distortions become more localized to the particle surface. As a result, the

interfacial deformations grow, with the Iso-N interface bulging upwards in the vicinity of the CL, right where the anchoring conflict lies. For high anchoring strengths ($w^* \gg 1$), a topological defect appears at the particle surface very close to the CL [Fig. 2(b)].

In the P configuration [Fig. 2(c)], for which there is no anchoring conflict with $\theta = 90°$ [Fig. 1(b)], the Iso-N interface remains nearly flat regardless of the anchoring strength. A topological defect of winding number $-1/2$ forms beneath the particle, in accordance with the imposed boundary conditions. The defect position, which depends primarily on the anchoring strength prescribed on the particle surface, is not sensitive to w^* for it is far from the Iso-N interface.

The interfacial deformations of Fig. 2(a) are quantified in Fig. 3 as a function of w^* for the H configuration. The interfacial distortion $\Delta y_I = y_{cl} - y_w$ is defined as the difference between the y-location of the interface at the CL (y_{cl}) and that at the bounding wall (y_w). We see that Δy_I first grows steeply for $w^* \lesssim 1$ before levelling off at larger values with a crossover region around $w^* \simeq 1$. We can account for these two regimes via a scaling argument based on the competition between the bulk elastic energy of the nematic LC and the surface energies involving both surface tension and anchoring. The details of the derivation are presented in appendix B. We show that

$$\Delta y_I = w^* L \sqrt{\frac{\sigma L}{L_1(1+w^*)}}\,, \tag{12}$$

where L is the box size [52]. Thus, for $w^* \ll 1$, i.e. in the weak anchoring regime, we have $\Delta y_I \approx w^* L\sqrt{\sigma L/L_1}$, indicating that Δy_I should be a linear function of w^*. In the strong anchoring regime, $w^* \gg 1$, and Eq. (12) yields $\Delta y \approx L\sqrt{w^*\sigma L/L_1}$, i.e. a square root profile is expected in this case. It follows that a crossover point at $w^* = 1$ naturally appears between these two limits. As can be seen from Fig. 3, these predictions are very well confirmed by the numerical data. The inset of Fig. 3 provides a zoomed-in view of the crossover region, which indeed occurs around $w^* = 1$.

Thus, our analysis shows that, for $w^* \gtrsim 1$, the system resolves the anchoring conflict at the CL by deforming substantially the interface. In this regime, the energetic penalty incurred by the deformed interface is less than the cost associated with bulk elastic distortions and to deviations from the prescribed anchoring orientation. In doing so, the total

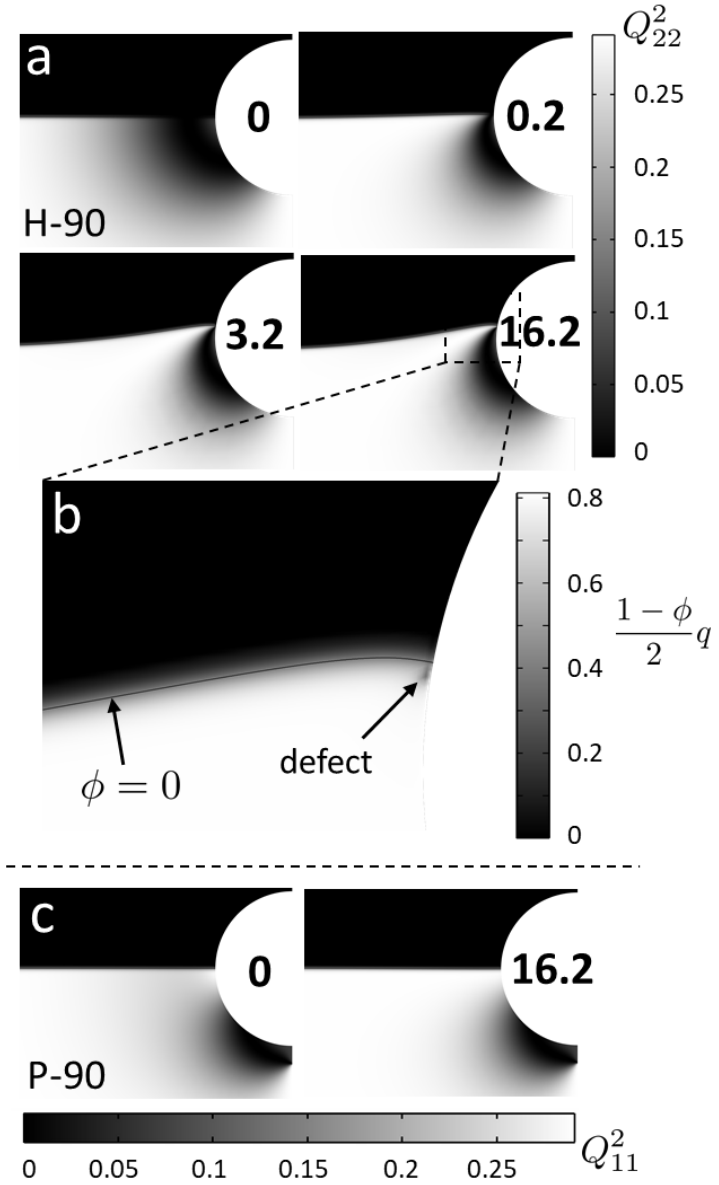

Figure 2: Zoomed-in snapshots computed at steady state with the anchoring strength w^* indicated in the white space inside the particle. The contact angle $\theta = 90°$ for all cases. **(a)** H configuration. Contour plots of Q_{22}^2. For $w^* = 16.2$, the dashed lines mark the cut-out area that is blown up in (b). **(b)** Zoomed-in view in the vicinity of the contact line for $w^* = 16.2$ in (a). The grey scale shows the concentration-weighted scalar order parameter $\frac{1-\phi}{2}q$, with $q_e = 0.81$. The small blurry dark spot signals a topological defect with $q \leqslant 0.5$. **(c)** P configuration. Contour plots of Q_{11}^2.

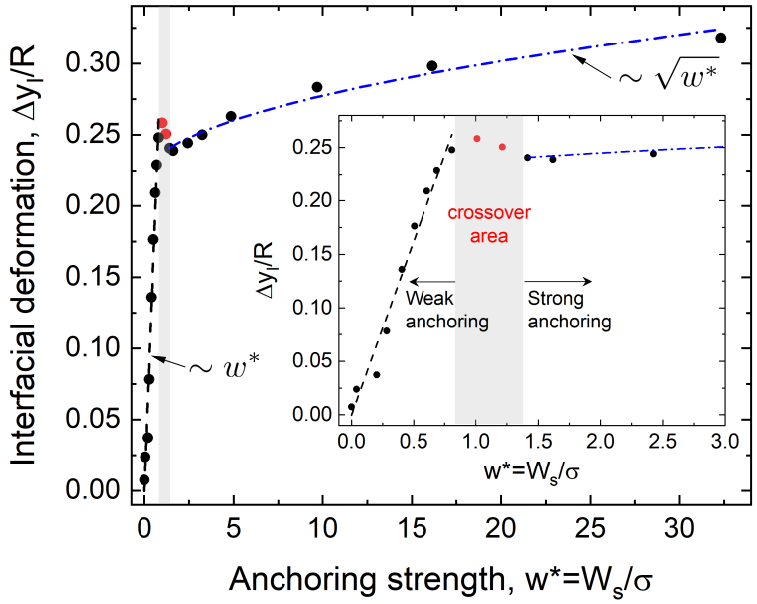

Figure 3: Interfacial deformation ($\Delta y_I/R$) as a function of the anchoring strength ($w^* = W_s/\sigma$) for the H configuration. The shaded area marks the transition between a steep initial variation (weak anchoring regime) and a milder increasing trend (strong anchoring regime). The black dashed (resp., blue dash-dotted) line is a linear (resp., square root) fit to the data [Eq. (12)]. The inserted graph is a zoomed-in plot of the crossover region around $w^* = 1$. The red data points lie within the crossover area and were not taken into account in the fitting procedure. Contact angle: $\theta = 90°$.

energy of the system is minimized. The fact that no interfacial deformation occurs in the P configuration [Fig. 2(c)], for which there is no anchoring conflict, is a further indication that the anchoring condition at the CL drives the response of the fluid interface to a large extent.

3.1.2 Free particle

In this section, we take into account the particle's equations of motion, which are solved with all the other governing equations, as outlined in Sec. 2.2. The particle is now free to move up or down depending on the forces acting on it. In turn, the shape of the Iso-N interface will be altered by the particle motion. We start with $\theta = 90°$ before considering other contact angle values.

Contact angle $\theta = 90°$. As before (Sec. 3.1.1), the particle's center of mass lies initially in the middle of the box and the fluid interface is flat, thereby realizing the condition $\theta = 90°$.

Typical results obtained at steady state are displayed in Fig. 4. In the H configuration [Fig. 4(a,b)], we see that the particle has now sunk into the N phase, with an appreciable downward particle displacement $d^* = d/R$. In this example, $d^* \simeq -0.3$ for $w^* = 0.5$. This displacement alters the shape of the Iso-N interface which no longer bulges upwards as before [Fig. 2(a)], but now bends downwards into a concave meniscus. With a freely moving particle, the system manages the anchoring conflict at the CL by pushing the particle into the N phase, which is also likely to result in less pronounced interfacial distortions. Thus, the particle position across the interface may be seen as a new degree of freedom that can be adjusted to minimize the overall energy. In contrast, the P-configuration of Fig. 4(c,d) hardly shows any interfacial deformation or particle displacement, even with a stronger anchoring ($w^* = 2$). This is because of the lack of an anchoring conflict at the contact line. Therefore, the extent of particle motion and interfacial deformations appear to be directly correlated to the existence of an anchoring conflict at the CL. In the following, we will test further this conjecture by employing other contact angles and various anchoring strengths in both H and P setups.

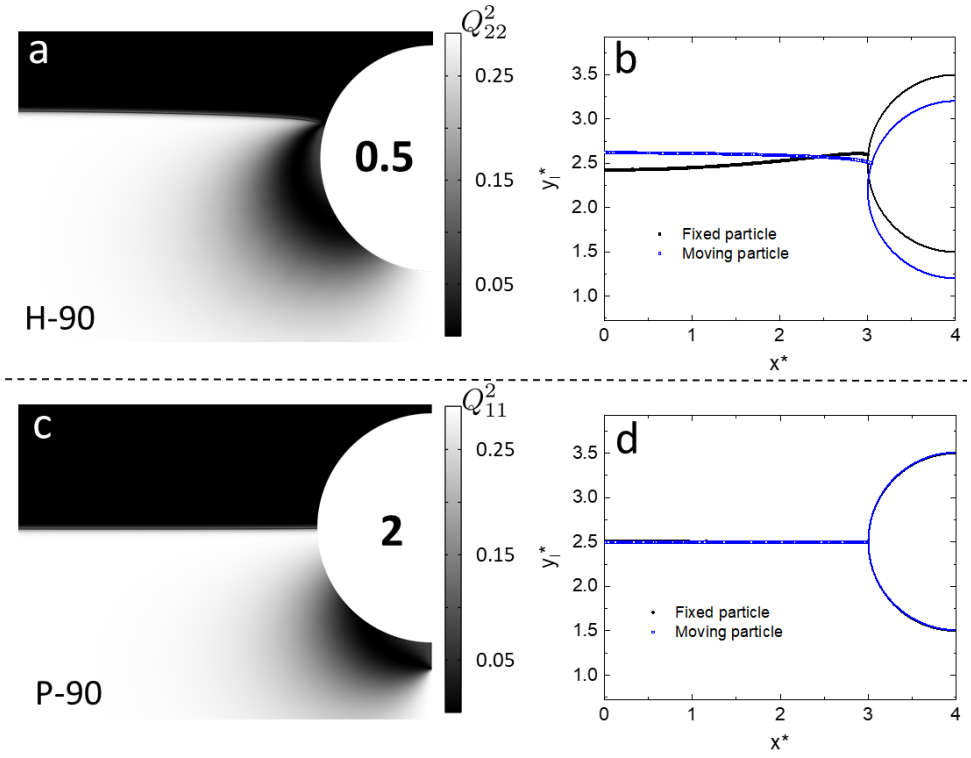

Figure 4: Order parameter snapshots and interfacial profiles with a moving particle. **(a,b)** H configuration. **(c,d)** P configuration. The bold black figures indicate the value of w^* in each case. (a) (resp., (c)) Contour plot of Q_{22}^2 (resp., Q_{11}^2). (b),(d) Comparison of interfacial profiles ($y_I^* = y_I/R$) computed in the fixed and moving particle cases ($x^* = x/R$). Contact angle: $\theta = 90^\circ$.

Contact angle $\theta \neq 90°$. We restrict our investigation to two distinct cases, one in which most of the particle body lies in the N phase ($\theta = 45°$), and another one for which the particle is preferentially immersed in the Iso phase ($\theta = 135°$). As previously, we will monitor the response of the system as we tune the anchoring strength at the Iso-N interface for both the H and P configurations.

We start with $\theta = 45°$ and the H configuration. The series of snapshots exhibited in Fig. 5 reveals an interesting phenomenon. For $w^* = 0$ [Fig. 5(a)], a topological defect of winding number $-1/2$ forms slightly below the equator of the particle as if it were repelled from the Iso-N interface. On the contrary, for a finite but weak anchoring strength [$w^* = 0.4$, Fig. 5(b)], the defect gets attracted towards the interface but stabilizes itself at an equilibrium distance from it. This attraction has an elastic origin and probably results from the onset of an anchoring conflict at the CL, where the $\mathbb{Q}$-field deformations differ greatly from the $w^* = 0$ case. Further increasing w^* leads to a stronger elastic attraction and eventually to the trapping of the defect within the interfacial area, very close to the CL [Fig. 5(c)]. The close-up view on Fig. 5(d) indeed shows that the defect has not disappeared. Also, notice the significant interfacial deformation together with the substantial sinking of the particle into the N phase.

Hence, for a high enough w^*, it becomes energetically favorable for the system to absorb the defect at the interface rather than to sustain it in the bulk with costly director disturbances. This result is a further illustration of an otherwise well-known coupling effect between bulk elastic distortions and surface anchoring strength encountered in LC colloids (see e.g., [1, 33]).

Other wetting configurations are presented in Fig. 6. All snapshots on the left side correspond to situations with $w^* = 0$, whereas those displayed on the right side are calculated for weak to intermediate anchoring strengths. For $w^* = 0$, there is no particle displacement, or only a minute one, and the Iso-N interface remains flat. This is in general not the case with $w^* \neq 0$. Note that an anchoring conflict now occurs in the P configuration since $\theta \neq 90°$. As aforementioned, the system resolves the anchoring conflict primarily by moving the particle across the Iso-N interface. In general, for a given

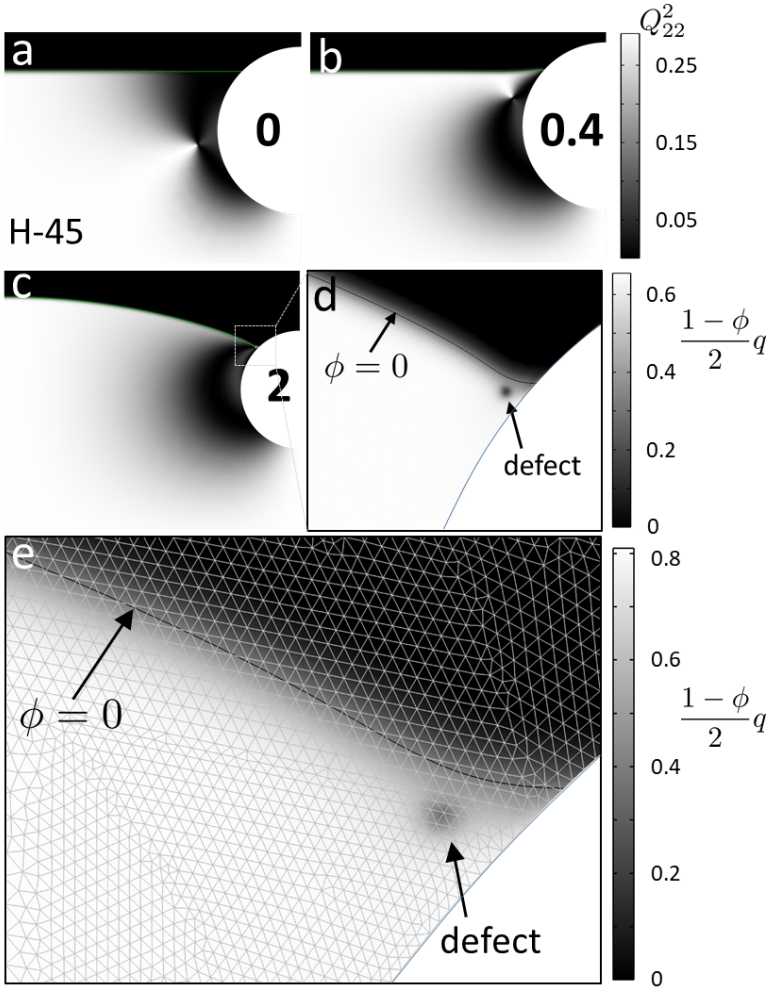

Figure 5: **(a-c)** Steady state wetting configurations obtained with a moving particle for several anchoring strengths (w^*, indicated by the bold black figures) in the H configuration with $\theta = 45°$. The particle displacement, $d^* = d/R$, is also specified hereafter: (a) $d^* = 2 \times 10^{-3}$, (b) $d^* = 0.05$, (c) $d^* = -0.5$. As w^* increases, the defect is elastically attracted towards the Iso-N interface close to the CL and eventually gets trapped there. The Iso-N interface also becomes more deformed due to a sizeable downward displacement of the particle. Grey scale: Q_{22}^2. **(d)** Close-up view of (c) near the contact line. Grey scale: $\frac{1-\phi}{2}q$. The dark blurry spot signals a topological defect lying within the interfacial area very close to the contact line. **(e)** Blown-up view of (d) showing a typical fine mesh in the vicinity of the interface ($\phi = 0$) and the topological defect. As mentioned in Sec. 2.4, the mesh gradually coarsens away from the interfacial area.

configuration (either H or P) and θ, the greater w^*, the larger the particle displacement. For example, in Fig. 6(b), the particle went up significantly ($d^* = 0.33$) and a sizeable interfacial deformation remains at equilibrium. However, bulk elastic disturbances are very moderate as they are localized in the close proximity of the CL and there is no longer any defect nearby the particle, in contrast to Fig. 5. Next, in Fig. 6(d), the particle has sunk substantially ($d^* = -0.37$) resulting in a slightly curved interface near the CL. This arises from an anchoring conflict at the CL, which is clearly signalled by additional elastic distortions of the $\mathbb{Q}$-field [compare Fig. 4(c) and Fig. 6(d)]. Finally, a nearly flat interface results in Fig. 6(f) with an upward motion of the particle ($d^* = 0.18$). Since only a small portion of the solid surface is submerged in the nematic, elastic distortion is limited to a small area, as compared with the case of $\theta = 90^\circ$ in Fig. 4(c). A defect of winding number $-1/2$ still lies beneath the particle, in agreement with the prescribed BCs.

To summarize, with finite anchoring on the Iso-N interface, potentially large interfacial deformations and particle displacements, on the order of $0.5R$, may occur whenever there is an anchoring conflict at the CL. This finding has never been predicted before nor observed in experiments, and is the central result of Problem A. It is a direct consequence of the coupling between elastic, capillary (surface tension) and anchoring effects.

3.2 Problem B: drag force

Problem B concerns the drag force on a particle straddling an Iso-N interface. As mentioned in the introduction, a few experiments have touched upon this topic [24, 28, 29] but no prior theoretical or computational work seems to have been reported so far.

Fig. 1(c) specifies the setup, as already described in Sec. 2.3. A 2D planar geometry is employed in order to first capture some main qualitative physical trends. As in Problem A, a rigid homeotropic anchoring is prescribed at the particle surface. To simplify the analysis of the drag force, we make two further adjustments of the parameters. We increase the surface tension by a factor of 10 relative to that of Problem A to minimize interfacial deformation (appendix A). Besides, we adopt the P-configuration with soft planar anchoring ($w^* = 0.4$) on the Iso-N interface to avoid complications from the an-

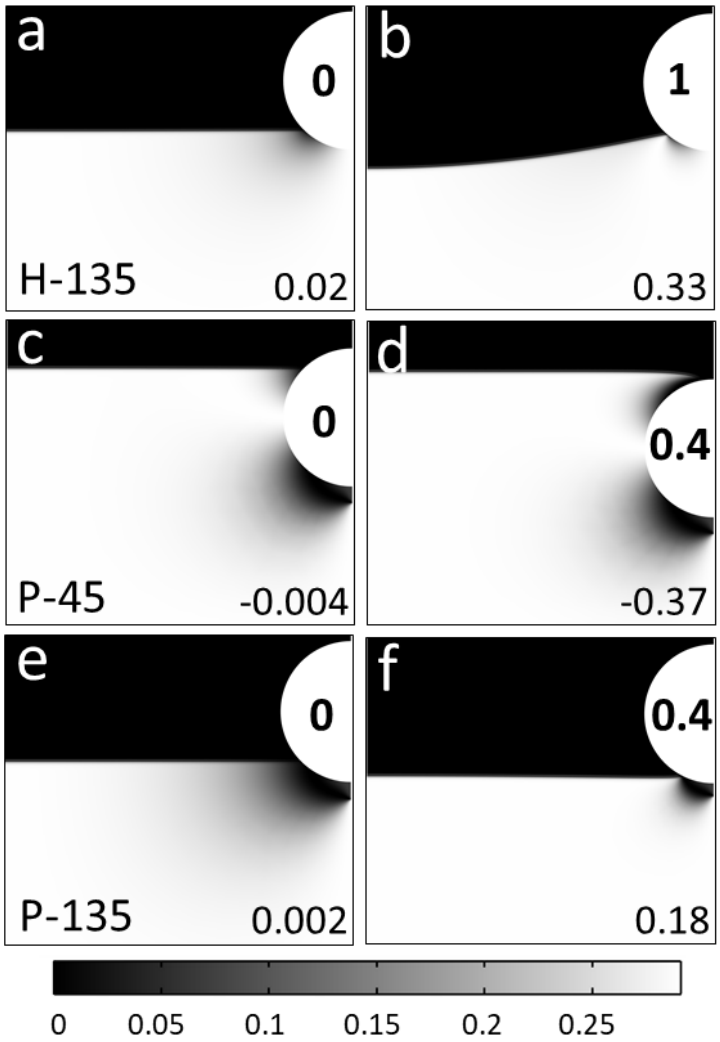

Figure 6: Additional steady state wetting configurations calculated with a moving particle. As in Fig. 5, the bold black figures (inside the particle) mark the values of w^* and d^* is also specified at the bottom right corner in each case. **(a,b)** H configuration, $\theta = 135^\circ$. **(c-f)** P configuration. (c,d) $\theta = 45^\circ$. (e,f) $\theta = 135^\circ$. Depending on θ and w^*, the particle goes either up or down with relatively small interfacial deformations, except in (b). Color bar: Q_{22}^2 (a,b), Q_{11}^2 (c,f).

choring conflict at the CL. In all cases, the motion of the particle is heavily overdamped since the Reynolds number $\mathrm{Re} = \rho_n v_\infty R/\eta_n$ is very small ($\lesssim 10^{-5}$, cf. appendix A). Furthermore, a moderate coupling between the fluid velocity and the $\mathbb{Q}$-field is considered with the Ericksen number Er in the range $0.28 - 3$ (cf. Sec. 2.3). Given the complexity of the problem and the large parameter space, we focus here on two key parameters, θ and Er . A more extensive exploration will be conducted in the future.

The drag force, $F_D^*(\mathrm{LC}) = F_D(\mathrm{LC})/L_1$, consists of the x-component of elastic and viscous forces, which are evaluated by integrating the corresponding tractions along the particle contour, as in Eq. (10). As a reference, the drag force for an isotropic-isotropic (Iso-Iso) interface, $F_D^*(\mathrm{iso})$, was also calculated with the fluids having the same viscosities as those of the Iso-N system. This force corresponds to the limit of $A, B, C, L_1, W_s \to 0$ (Sec. 2.1) and thus only contains a viscous component. In the next two sections, we investigate the influence of θ and Er on $F_D^*(\mathrm{LC})$.

3.2.1 Influence of the contact angle θ

Fig. 7(a) shows the drag force as a function of the contact angle ($[45° - 135°]$) at two values of Er . For convenience, we have used the ratio $\tilde{F}_D = F_D^*(\mathrm{LC})/F_D^*(\mathrm{iso})$ to assess the influence of the nematic ordering around the particle on the drag force. Note that the interface is maintained flat by shifting the center of the particle across the Iso-N interface. Gray scale plots of Q_{11}^2 show some illustrative steady [Fig. 7(b,c)] and transient [Fig. 7(d,e)] states obtained for a few θ values.

We first notice that the curve $\tilde{F}_D = f(\theta)$ [Fig. 7(a)] is asymmetric with respect to $\theta = 90°$. This is of course expected since the Iso-N interface breaks the up-down symmetry. We checked that for an Iso-Iso interface with matched viscosities between the two fluids, the curve $\tilde{F}_D = f(\theta)$ has the shape of a symmetric concave parabola, in agreement with previous results [48, 53]. Second, for both Er values, we see that $\tilde{F}_D > 1$ in most cases, and notably, $\tilde{F}_D$ is maximum for $\theta \simeq 50°$, i.e. when most of the particle body is immersed into the N phase [Fig. 7(c)]. In this case, the distorted nematic texture [see e.g., Fig. 7(b,c)] increases the drag force by about $15 - 20\,\%$ compared to a purely

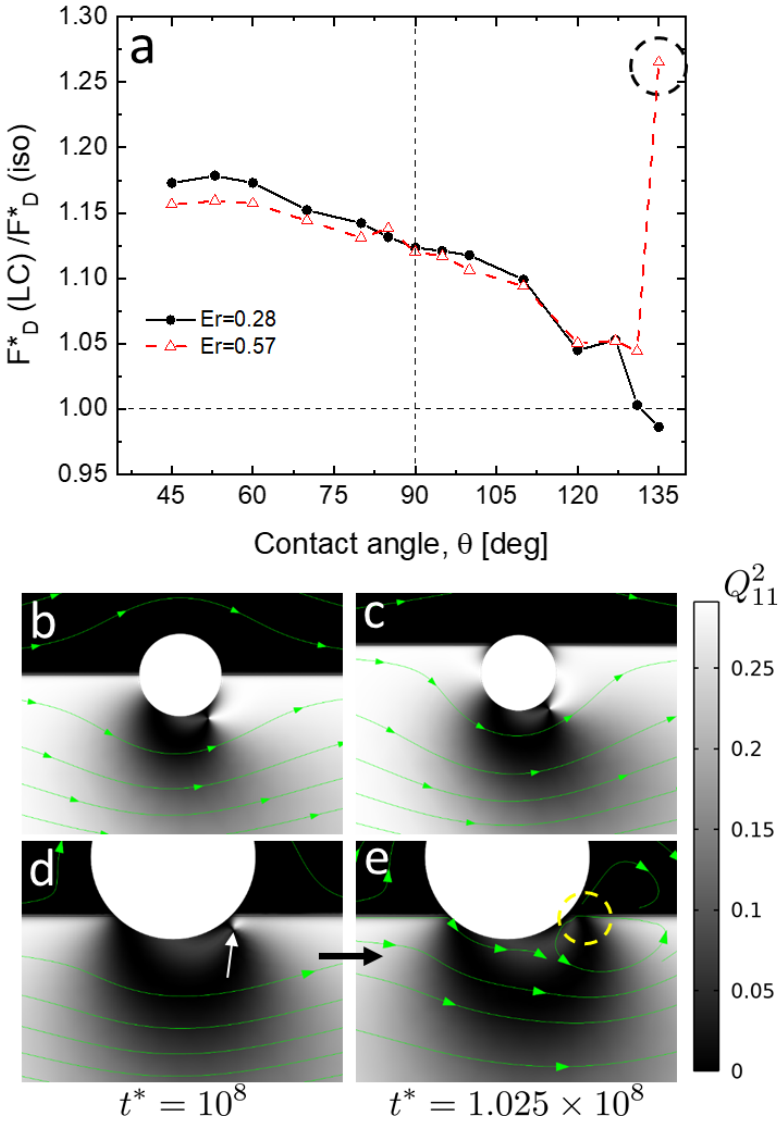

Figure 7: (Problem B) Results of drag simulations for various contact angles and a flat interface in the P configuration. **(a)** Normalized drag force $F_D^*(\mathrm{LC})/F_D^*(\mathrm{iso})$ as a function of θ for Er $= 0.28, 0.57$. **(b)-(e)** Flow and nematic fields for different contact angles and Er $= 0.57$. (b) Steady state for $\theta = 90°$. (c) Steady state for $\theta = 45°$. (d,e) Transient states for $\theta = 135°$. $t^* = t/\tau$ indicates the simulation time. In this case, we see that the defect, marked by the white arrow in (d), merges with the interface as a result of both flow advection and an attractive elastic interaction (see text for details). After the merging (cf. dashed circle in (e)), the system remains in this state till the end ($t^*_{\mathrm{end}} = 2 \times 10^8$). Gray scale: Q^2_{11}. Bright (resp., dark) areas correspond to LC molecules aligned parallel (resp., perpendicular) to the horizontal axis (same meaning hereafter). The green arrow lines represent the flow streamlines.

isotropic system. This drag enhancement may be explained by the fact that the fluid has to flow through distorted regions of the nematic field where the orientation of LC molecules changes. This is especially true near topological defects where large gradients of the order parameter usually occur. Reorientations of mesogens bring up an additional contribution to F_D^*(LC) via the rotational viscosity γ_1 (Sec. 2.3) [10], which is specific to nematics. Heuristically, we may imagine that the particle and its companion defect [e.g., Fig. 7(b)] form a bigger effective particle in the N phase that has to be dragged along, thereby enhancing the friction.

Besides, we see that the main effect of the imposed external flow is to shift the topological defect downstream of the particle, to a steady state position if Er is not too large [Fig. 7(b,c)]. At this relatively low Er, the viscous forces from the fluid flow are strong enough to alter the orientation of LC molecules and yield a modified nematic texture. This is a prominent feature of the coupling between the flow and the LC orientation. Note that similar defect motions in bulk LC colloids were reported for Er ~ 1 [54, 55, 56, 57].

Next, as θ increases [Fig. 7(a)], $\tilde{F}_D$ decreases and tends towards unity, which goes in line with intuition since the particle is more exposed to the isotropic phase in this case. However, an anomaly occurs for Er $= 0.57$ and $\theta = 135°$ as $\tilde{F}_D$ jumps to a larger value (cf. dashed circle). This phenomenon may be ascribed to the merging of the defect with the Iso-N interface [Fig. 7(d,e)], which induces the formation of a pair of small vortices on either side of the interface downstream of the particle [see Fig. 7(e)]. These vortices originate from a Marangoni flow that develops along the interface because of the existence of an anchoring energy gradient near the contact line, as demonstrated in Fig. 8. Close to the contact line, the fluids flow along the interface from locations of low anchoring energy to those of high anchoring energy, in agreement with Rey's theory on Marangoni flow at LC interfaces [58]. This anchoring energy gradient arises from the disturbed molecular orientation in this area as a consequence of the defect-interface merging. Note that the defect has disappeared from the interfacial area, giving rise to a nonsingular configuration. The Marangoni eddies persist over long times and might be responsible for the enhanced drag force exerted on the particle in this case.

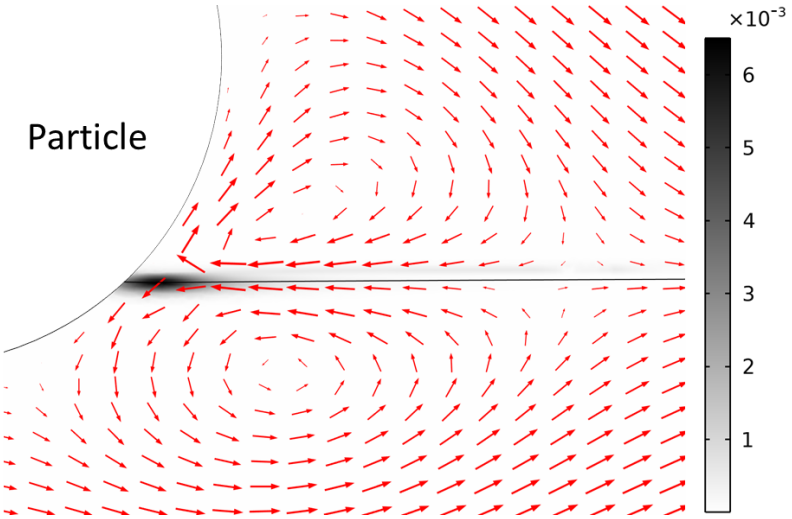

Figure 8: (Problem B) Zoomed-in view of Fig. 7(e) near the contact line downstream of the particle. The gray scale shows the dimensionless anchoring energy density, $f_a^* = f_a/(L_1 l_{\rm nc})$, which is defined across the entire diffuse interface [Eq. (3)]. As such, we see that it spreads both below and above the level set $\phi = 0$. The arrows indicate the velocity field. The anchoring energy gradient close to the contact line drives a Marangoni flow that is signaled by a pair of vortices located on either side of the interface (solid curve). These vortices may increase the drag force exerted on the particle. Parameters: Er $= 0.57$, $\theta = 135°$.

The merging of the defect with the interface [Fig. 7(d,e)] may be caused by the combination of two effects: advection and elastic attraction. The merging only occurs for $\mathrm{Er} = 0.57$ but not for $\mathrm{Er} = 0.28$. In the former case, the flow is strong enough to sweep the defect sufficiently close to the interface so that it falls within the range of an attractive elastic interaction there. Indeed, from the dynamic motion of the defect [Figs. 7(d,e)], it seems as if it is captured by the interface. This phenomenon appears consistent with what we reported previously in Fig. 5, where a defect trapping occurs, although in the absence of external flow.

3.2.2 Influence of the Ericksen number

In this section, we address in more detail the influence of the Ericksen number on the drag force [Fig. 1(b)]. In Sec. 3.2.1, only two different values of Er were considered for a broad range of θ (Fig. 7). Here, we carry out a complementary study and vary Er more systematically for only two different values of θ. Besides, the particle's center of mass is now kept fixed midway across the interface. Thus, the case $\theta = 90^\circ$ yields a flat interface, as before (Sec. 3.2.1), but a nonflat interface results if $\theta \neq 90^\circ$. The latter setup is useful to examine the effect of interfacial deformations on the drag force. The numerical setup is exactly the same as before [Fig. 1(c)].

Contact angle $\theta = 90^\circ$. Fig. 9(a) summarizes the results of our drag force computations for $\theta = 90^\circ$ as a function of the dimensionless far-field imposed velocity $v_\infty^* = \tau v_\infty / l_{\mathrm{nc}}$, where l_{nc} is the nematic coherence length and τ a typical molecular time (see appendix A). For the Iso-N interface, the maximum value of v_∞^* corresponds to $\mathrm{Er} = 1.71$. We could not investigate larger Er values here because, for $\mathrm{Er} \geqslant 1.71$, the defect 'escapes' from the particle and gets convected downstream continually by the flow, as shown in Fig. 9(b,c). Even though no steady state can be reached in this case, the drag force acting on the particle remains about constant once the defect is sufficiently away from it. Previous 3D studies in bulk LC colloids reported similar defect detachments under the influence of flow [54, 57]. As in our study, it was found that defect separation typically occurs for $\mathrm{Er} \gtrsim 1$, i.e. when the viscous forces become stronger than elastic forces. Otherwise

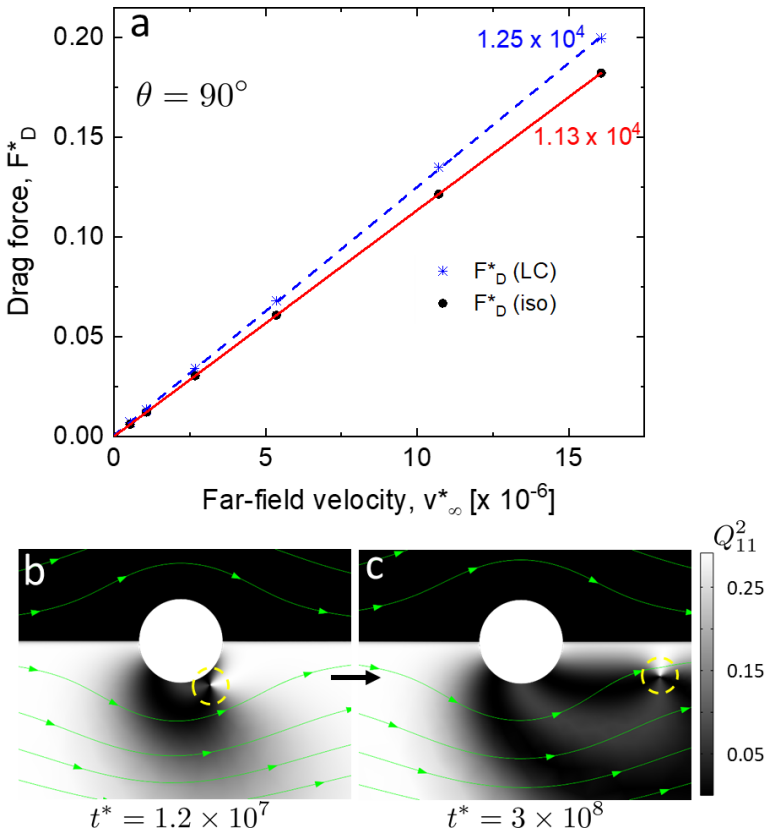

Figure 9: (Problem B) P configuration, $\theta = 90°$. **(a)** Drag force (F_D^*) as a function of the prescribed far-field velocity (v_∞^*) for both the Iso-N and Iso-Iso interfaces. The solid and dashed lines are linear fits to the data. The numbers next to the fitting lines indicate the corresponding slopes. **(b,c)** Transient snapshots (gray scale: Q_{11}^2) of the Iso-N interface illustrating the defect escape from the particle for the last data point on (a) corresponding to Er $= 1.71$. The defect, marked by the dashed yellow circle, is swept downstream by the flow, whose streamlines are represented by green arrow lines. The defect is still located close to the particle at time $t^* = 1.2 \times 10^7$ (b) but is being driven away from it at later times (c).

stated, since the defect motion is governed by director rotation, the defect abandons the particle when the elastic torque can no longer prevent the director from rotating under the viscous torque due to the passing flow. In Fig. 9(c), notice the sizeable spatial extension of $\mathbb{Q}$-distortions (dark areas) induced by the flow.

In addition, the graph on Fig. 9(a) clearly reveals a proportionality between F_D^* and v_∞ in both the Iso-Iso and Iso-N cases. While the linear behavior was expected in the isotropic situation (Reynolds number $\mathrm{Re} = \rho_n v_\infty R/\eta_n \lesssim 10^{-5}$), it was not guaranteed, a priori, that linearity would hold as well for the Iso-N interface in a regime where Er is not particularly small ($\mathrm{Er} \sim 1$). As far as we know, nonlinear drag forces were only reported by Stark & Ventzki [59] for a spherical particle exhibiting the dipolar configuration in a bulk nematic matrix.

Moreover, we see that the friction coefficient, F_D^*/v_∞^*, which is given by the slope of linear fits in Fig. 9(a), is slightly larger in the Iso-N case than in the Iso-Iso case. This result can be explained via the same arguments as those put forward previously (Sec. 3.2.1): as v_∞ increases, areas where the nematic alignment is distorted grow in size as a result of the coupling between the velocity and order parameter fields. Advection of the defect is also more pronounced, leading to significant molecular reorientations which contribute to the friction through the rotational viscosity.

Contact angle $\theta = 135°$, nonflat interface. Finally, we consider the case of a nonflat interface by setting $\theta = 135°$. Since the particle's center of mass is fixed, the Iso-N interface now deforms downwards so that most of the particle body is exposed to the isotropic phase. The graph in Fig. 10(a) compares the drag force data obtained in this configuration for the Iso-N and Iso-Iso interfaces, similarly to Fig. 9(a). First, in the Iso-Iso case, the friction coefficient (slope of the linear fit) is slightly larger than its counterpart determined in Fig. 9(a) for a flat interface (1.2×10^{-4} vs. 1.1×10^{-4}, respectively). This result agrees with our previous findings that a deformed fluid interface breaks the up-down symmetry and leads to more bending of the flow streamlines, which enhances the friction and the drag coefficient [48]. Second, in the Iso-N case, we observe again a linear relationship between F_D^* and v_∞^*. This linearity prevails up to $\mathrm{Er} = 2.86$, corresponding to

the maximum v^*_∞ in the graph. As before, the friction coefficient for the Iso-N interface is slightly larger than that of the Iso-Iso interface, most likely for the same reasons as those already mentioned in the flat interface situation [Fig. 9(a)].

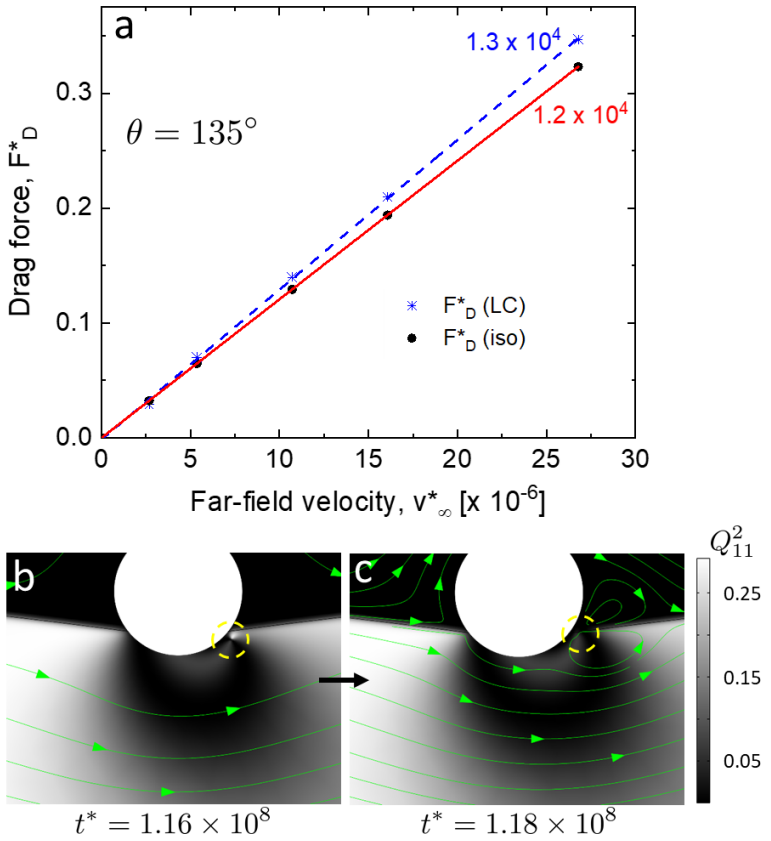

Figure 10: (Problem B) P configuration, $\theta = 135°$. **(a)** Same as in Fig. 9(a). **(b,c)** Transient zoomed-in snapshots (Gray scale: Q^2_{11}) illustrating the merging of the defect with the Iso-N interface for $\mathrm{Er} = 0.57$. The yellow dashed circle marks the defect location just before (b) and right after (c) the merging event. The green arrow lines represent the streamlines and t^* is the simulation time.

However, Fig. 10 does show a distinct feature. The defect does not escape from the particle as observed before with $\theta = 90°$ and $\mathrm{Er} \geqslant 1.71$ [Fig. 9(c)]. Instead, it merges with the Iso-N interface for $\mathrm{Er} \geqslant 0.57$, as illustrated in Fig. 10(b,c). Since the interface is now bent downwards, the flow can sweep the defect closer to it so that, at some point, an attractive elastic interaction between the defect and the interface, already encountered in

Fig. 5 and Fig. 7(d,e), takes over and results in the trapping of the defect. As in Fig. 7(e), the defect disappears from the interfacial region once adsorbed, giving rise to a pair of Marangoni vortices located on either side of the interface [Fig. 10(c)]. The defect merging, as explained before, is expected to cause additional drag [Fig. 7(a)]. In fact, this seems to be the case in Fig. 10(a) as well. The merging does not occur for the first data point of Fig. 10(a) at $v_\infty^* = 2.7 \times 10^{-6}$ and Er $= 0.28$, but occurs for all the higher values of Er. The first data point falls a bit below the linear relationship manifested by the higher-Er data points by some 15% . This is less than the amount of drag enhancement ($\simeq 28\%$) observed in Fig. 7(a) due to defect merging but the two configurations are different.

4 Concluding remarks

We have performed numerical simulations on the behavior of solid colloidal particles attached to an Iso-N fluid interface. Building on our previous work, we have employed a model that combines a diffuse interface method (phase-field) to account for the properties of the Iso-N interface with a tensor order parameter description of the nematic phase, including topological defects. Such a model is well suited to describe elastocapillary phenomena, i.e. situations involving a coupling between elasticity and capillarity. We have first focused our attention on equilibrium floating configurations for both homeotropic and planar anchoring types at the Iso-N interface with various anchoring strengths and contact angles. A rigid homeotropic anchoring was assumed at the particle surface in all cases. One of the key findings is that the anchoring conditions at the contact line drive the response of the system in terms of interfacial deformations and/or particle displacements. We have discovered two regimes with two distinct scaling laws for the magnitude of interfacial distortions. A strong anchoring conflict generally yields a sizeable particle shift and interfacial deformation. Note that, because of their negligible buoyant weight, the particle we considered would not produce any interfacial distortion if adsorbed at isotropic planar interfaces. Thus, our results bring up the novelty of the Iso-N interface and highlight the interplay between elastic distortions, surface tension and the anchoring conditions.

In the second part, we have studied the dynamic situation of a particle being dragged along an interface. One of the primary objectives was to assess the influence of elastic distortions on the drag force exerted on the particle, and more generally, the effect of the coupling between the velocity and order parameter fields. We have computed drag forces as a function of the contact angle and the Ericksen number. Only a moderate planar anchoring has been considered at the Iso-N interface. Our investigation reveals that (i) drag forces at the Iso-N interface are always greater, albeit only slightly, than their isotropic counterparts and (ii) generally, greater drag enhancement tends to occur for smaller contact angles, when more of the particle body is immersed in the N phase. Defect sweeping, escaping, and merging with the interface, together with large distorted areas of the order parameter, contribute to the drag enhancement. For both flat and nonflat interfaces, the drag force is linearly proportional to the velocity in the entire range examined, up to Ericksen numbers of order unity.

The current 2D implementation of our model may be extended to address the case of a sphere trapped at the I-N interface in 3D, which can be more directly compared with experiments. Preliminary simulations of a floating sphere carried out in a 2D-axisymmetric geometry confirm qualitatively the main findings of the present 2D study: the presence of conflicting anchoring conditions at the contact line is responsible for the onset of interfacial deformations, and the stronger the anchoring, the greater the distortions. A detailed study will be reported in a forthcoming article. However, the computation of drag forces acting on a sphere straddling the I-N interface requires a full three-dimensional approach, which cannot be tackled yet by our current model implementation. Nevertheless, prior studies in bulk nematics [54, 55, 56, 57] suggest that line defects may be distorted by the passing flow, detach from the particle, shrink or even transform into a point. As in the 2D case, defects merging with the interface could also be expected. These phenomena, if they occur, are likely to alter drag forces and perhaps make the force-velocity law deviate from a linear behavior.

Our two-dimensional results also form the basis for exploring more complex situations such as multiparticle interactions based on the elastocapillary coupling. Indeed, we have

shown that sizeable interfacial deformations may take place due to the interplay of elastic and anchoring effects. Thus, in principle, we may expect the capillary and elastic interactions to contribute simultaneously to the self-assembly properties of the system. As mentioned in the introduction, a number of experimental and theoretical studies shed some light on this topic over the past few years [17, 20, 21, 32], but there is still no clear demonstrations of the interaction mechanisms by accurate computations. We currently focus our simulation efforts in this direction.

Acknowledgements

This work was financially supported by the EU Marie-Curie fellowship 'CoPEC' under grant No 794837–H2020-MSCA-IF-2017 and by the NSERC Discovery grant No 2019-04162. J.-C.L. is also indebted to the University of Bordeaux for further financial support thanks to the IdEx program entitled "Développement des carrières - Volet personnel de recherche". M.Q. acknowledges support from the UBC Four-year Doctoral Fellowship. A.C. was supported by an overseas visiting doctoral fellowship from SERB, Department of Science & Technology, Government of India. We acknowledge CMC Microsystems for software licensing. The IT staff of the Mathematics department of the University of British Columbia is also gratefully acknowledged for their valuable help and support.

Appendix A Simulation parameters

The parameters characterizing the nematic LC are close to those of the widely used compound 5CB [42, 60, 61]. The numerical parameters for the CH dynamics (capillary width ϵ, mobility γ) are chosen according to the guidelines reported in [38, 44, 45]. The dimensional base values of all simulation parameters are listed in the following table.

Table 1: Definitions and base values of the parameters used in the simulations. The subscript "n" (resp., "i") stands for nematic (resp., isotropic). The superscript A (resp., B) refers to problem A (resp., B). "PS" is the abbreviation for Phase-Field.

Parameter	Symbol	Value	Unit
Elastic constant	L_1	10	pN
Landau-de Gennes coefficients	A	-10^5	Pa
	$B = -C$	-6×10^5	Pa
Scalar order parameter at equilibrium	q_e	0.81 [33]	-
Nematic coherence length	$l_{\rm nc} = \sqrt{\frac{L_1}{\lvert A \rvert}}$	10	nm
Typical molecular time	τ	1	ns
Nematic shape factor	ξ	0.6	-
Nematic rotational viscosity	$\gamma_1 = 1/\Gamma$	0.04	Pa.s
Density	$\rho_n\,, \rho_i$	10^3	kg.m^{-3}
Viscosity	$\eta_n\,, \eta_i$	0.07	Pa.s
Surface tension	σ	$10^{-3\,(A)}$, $0.01^{(B)}$	N.m^{-1}
Anchoring strength	W_s	$0 - 0.016$	N.m^{-1}
Particle radius	R	1	μm
Contact angle	α	$45° - 135°$	deg
Capillary width (PS)	ϵ	$20^{(A)}$, $40^{(B)}$	nm
Mobility (PS)	γ	4×10^{-15}	m^2/(Pa.s)
Far-field velocity	v_∞	$27 - 270$	μm.s^{-1}
Box dimensions (height,length)	(H, L)	$(8R, 10R)^{(A)}$, $(20R, 30R)^{(B)}$	μm

Appendix B Derivation of [Eq. (12)]

We derive Eq. (12) using simple scaling arguments based on the competition between the bulk elastic energy of the nematic LC and the surface energies (surface tension and anchoring).

Fig. 11 specifies the geometry for our reasoning. To derive Eq. (12), there is no need to consider explicitly a particle attached to the interface (actually, the particle size is not a relevant length scale of the problem). The right wall of the box 'stands for' the particle surface and we assume that an anchoring conflict exists there resulting in a deformed interface (dashed curve in Fig. 11). The typical interfacial deformation is denoted Δy_I .

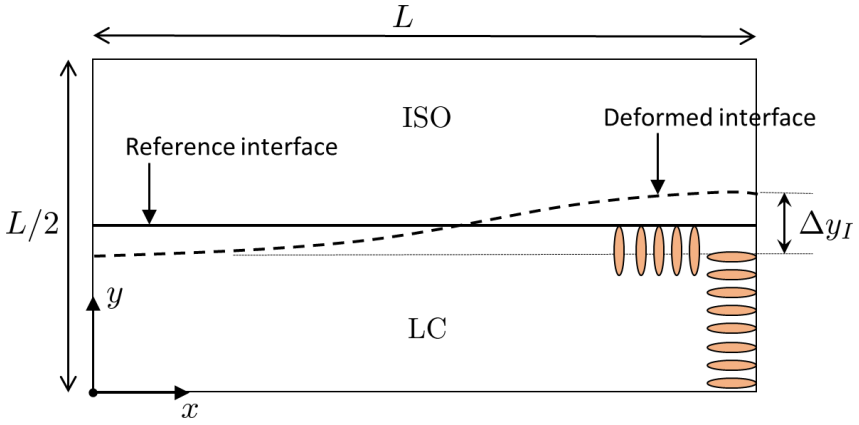

Figure 11: Geometry used for the scaling argument. The right boundary symbolizes the particle surface in the actual simulation. The small ellipsoids represent the LC molecules (not to scale). We assume they are oriented parallel to the y-axis everywhere except at the right wall. These conditions result in an anchoring conflict of the H type there [Fig. 1(b)], which makes the Iso-N interface bulge upwards.

Bulk elastic energy - As a first approximation, we know that the elastic free energy density, f_e , scales as $\sim L_1/\xi^2$, where $L_1 = K/q_e^2$ (Sec. 2.3) is proportional to the elastic constant K of the nematic LC, and ξ is the characteristic length scale of the director deformations. In the presence of a finite anchoring strength W at the Iso-N interface, we may take $\xi \sim L_W = L_1/W$, where L_W is the anchoring extrapolation length. Indeed, this is the relevant characteristic length to describe director deformations due to an anchoring

conflict (cf. Fig. 11). It follows that the change in the elastic energy density due to a nonzero anchoring strength can be written as $\delta f_e \sim W^2/L_1$. Furthermore, assuming that the area $A \sim L^2$ of the nematic domain remains about constant (small variation), the change in the elastic energy reads

$$\delta F_e \sim \frac{W^2}{L_1} A \,. \tag{B.1}$$

Surface energies - In order to estimate the change in surface energies, we have to compute the excess length δL of a deformed interface caused by the existence of an anchoring conflict. The resulting excess surface energy is simply given by $\delta F_s = (\sigma + W)\delta L$ since both interfacial and anchoring energies will be affected by a change in L.

From simple considerations of differential calculus, we have $dL' = dL\sqrt{1 + (dy/dx)^2}$, where dL' is a length element of the deformed interface and dL its projection along the x-axis. Assuming small interfacial deformations, and hence small slopes ($(dy/dx) \ll 1$), we may write $dL' \approx dL\left[1 + \frac{1}{2}(dy/dx)^2\right]$ resulting in $\delta(dL) = dL' - dL = \frac{1}{2}(dy/dx)^2 dx$. In terms of orders of magnitude, $(dy/dx) \sim \Delta y_I / L$, leading to $\delta L \approx \left(\frac{\Delta y_I}{L}\right)^2 \int_0^L dx = \frac{\Delta y_I^2}{L}$, where the (unimportant) prefactor 1/2 has been dropped. Consequently, we may write

$$\delta F_s \sim (\sigma + W)\frac{\Delta y_I^2}{L} \,. \tag{B.2}$$

Balancing the two Eqs. (B.1) and (B.2) yields Eq. (12)

$$\Delta y_I = w^* L \sqrt{\frac{\sigma L}{L_1(1 + w^*)}} \,.$$

Author contribution statement

J-CL and JJF designed the research. J-CL and AC performed the work; all authors analyzed the data, interpreted the results and collaborated to the manuscript written by J-CL.

References

[1] I. I. Smalyukh, Liquid crystal colloids, Annu. Rev. Condens. Matter Phys. 9, 207-226 (2018).

[2] R. McGorty, J. Fung, D. Kaz, V. N. Manoharan, Colloidal self-assembly at an interface, Materials Today 13, 34-42 (2010).

[3] P. Poulin, H. Stark, T. C. Lubensky, D. A. Weitz, Novel colloidal interactions in anisotropic fluids, Science 275, 1770-1773 (1997).

[4] T. C. Lubensky, D. Pettey, N. Currier, H. Stark, Topological defects and interactions in nematic emulsions, Phys. Rev. E 57, 610-625 (1998).

[5] J.-C. Loudet, P. Barois, P. Auroy, P. Keller, H. Richard, P. Poulin, Colloidal structures from bulk demixing in liquid crystals, Langmuir 20, 11336-11347 (2004).

[6] I. Muševič, M. Škarabot, U. Tkalec, M. Ravnik, S. Žumer, Two-dimensional nematic colloidal crystals self-assembled by topological defects, Science 313, 954-958 (2006).

[7] M. Ravnik, M. Škarabot, S. Žumer, U. Tkalec, I. Poberaj, D. Babič, N. Osterman, I. Muševič, Entangled nematic colloidal dimers and wires, Phys. Rev. Lett. 99, 247801-1–4 (2007).

[8] U. Tkalec, S. Čopar, M. Ravnik, S. Žumer, I. Muševič, Reconfigurable knots and links in chiral nematic colloids, Science 333, 62-65 (2011).

[9] C. Blanc, D. Coursault, E. Lacaze, Ordering nano- and microparticles assemblies with liquid crystals, Liq. Crys. Rev. 1, 83-109 (2013).

[10] G. Foffano, J. S. Lintuvuori, A. Tiribocchi, D. Marenduzzo, The dynamics of colloidal inclusions in liquid crystals: a simulation perspective, Liq. Crys. Rev. 2, 1-27 (2014).

[11] P. A. Kralchevsky, K. Nagayama, Capillary interactions between particles bound to interfaces, liquid films and biomembranes, Adv. Coll. Int. Sci. 85, 145-192 (2000).

[12] M. Oettel, S. Dietrich, Capillary interactions at fluid interfaces, Langmuir 24, 1425-1441 (2008).

[13] K. D. Danov, P. A. Kralchevsky, Capillary forces between particles at a liquid interface: General theoretical approach and interactions between capillary multipoles, Adv. Coll. Interf. Sci. 154, 91-103 (2010).

[14] L. Botto, E. P. Lewandowski, Jr. M. Cavallaro, K. J. Stebe, Capillary interactions between anisotropic particles, Soft Matter 8, 9957-9971 (2012).

[15] S. Dasgupta, T. Auth, G. Gompper, Nano- and microparticles at fluid and biological interfaces, J. Phys.: Condens. Matter 29, 373003-1–41 (2017).

[16] I. B. Liu, N. Sharifi-Mood, K. J. Stebe, Capillary assembly of colloids: Interactions on planar and curved interfaces, Annu. Rev. Condens. Matter Phys. 9, 283-305 (2018).

[17] I. I. Smalyukh, S. Chernyshuk, B. I. Lev, A. B. Nych, U. Ognysta, V. G. Nazarenko, O. D. Lavrentovich, Ordered droplet structures at the liquid crystal surface and elastic-capillary interactions, Phys. Rev. Lett. 93, 117801-1–4 (2004).

[18] A. B. Nych, U. M. Ognysta, V. M. Pergamenshchik, B. I. Lev, V. G. Nazarenko, I. Muševič, M. Škarabot, O. D. Lavrentovich, Coexistence of two colloidal crystals at the nematic-liquid-crystal–air interface, Phys. Rev. Lett. 98, 057801-1–4 (2007).

[19] T. Yamamoto, M. Yoshida, Self-assembled pseudo-hexagonal structures of colloidal particles at air–liquid crystal interface, Appl. Phys. Express 2, 101501-1–3 (2009).

[20] M. A. Gharbi, M. Nobili, M. In, G. Prévot, P. Galatola, J. B. Fournier, C. Blanc, Behavior of colloidal particles at a nematic liquid crystal interface, Soft Matter 7, 1467-1471 (2011).

[21] N. Wang, J. S. Evans, C. Li, V. M. Pergamenshchik, I. I. Smalyukh, S. He, Controlled multistep self-assembling of colloidal droplets at a nematic liquid Crystal–air interface, Phys. Rev. Lett. 123, 087801-1–5 (2019).

[22] I. H. Lin, Jr. G. M. Koenig, J. J. de Pablo, N. L. Abbott, Ordering of Solid Microparticles at Liquid Crystal-Water Interfaces, J. Phys. Chem B 112, 16552-16558 (2008).

[23] Jr. G. M. Koenig, I. H. Lin, N. L. Abbott, Chemoresponsive assemblies of microparticles at liquid crystalline interfaces, Proc. Natl. Acad. Sci. U.S.A. 107, 3998-4003 (2010).

[24] I. B. Liu, M. A. Gharbi, V. L. Ngo, R. D. Kamien, S. Yang, K. J. Stebe, Elastocapillary interactions on nematic films, Proc. Natl. Acad. Sci. U.S.A. 112, 6336-6340 (2015).

[25] H. Jeridi, M. A. Gharbi, T. Othman, C. Blanc, Capillary-induced giant elastic dipoles in thin nematic films, Proc. Natl. Acad. Sci. U.S.A. 112, 14771-14776 (2015).

[26] H. Jeridi, M. Tasinkevych, T. Othman, C. Blanc, Colloidal particles in thin nematic wetting films, Langmuir 32, 9097-9107 (2016).

[27] M. A. Gharbi, D. Seč, T. Lopez-Leon, M. Nobili, M. Ravnik, S. Žumer, C. Blanc, Microparticles confined to a nematic liquid crystal shell, Soft Matter 9, 6911-6920 (2013).

[28] D. Abras, G. Pranami, N. L. Abbott, The mobilities of micro- and nano-particles at interfaces of nematic liquid crystals, Soft Matter 8, 2026-2035 (2012).

[29] W. S. Wei, M. A. Gharbi, M. A. Lohr, T. Still, M. D. Gratale, T. C. Lubensky, K. J. Stebe, A. G. Yodh, Dynamics of ordered colloidal particle monolayers at nematic liquid crystal interfaces, Soft Matter 12, 4715-4724 (2016).

[30] D. Andrienko, M. Tasinkevych, S. Dietrich, Effective pair interactions between colloidal particles at a nematic-isotropic interface, Europhys. Lett. 70, 95-101 (2005).

[31] M. Tasinkevych, D. Andrienko, Colloidal particles in liquid crystal films and at interfaces, Cond. Mat. Phys. 13, 33603-1–20 (2010).

[32] M. Oettel, A. Domínguez, M. Tasinkevych, S. Dietrich, Effective interactions of colloids on nematic films, Eur. Phys. J. E 28, 99-111 (2009).

[33] M. Qiu, J. J. Feng, J.-C. Loudet, Phase-field model for elastocapillary flows of liquid crystals, Phys. Rev. E 103, 022706-1–14 (2021).

[34] M. Qiu, Computational studies on interfacial dynamics in complex fluids, Ph.D thesis, University of British Columbia, 2020, `https://open.library.ubc.ca/cIRcle/collections/ubctheses/24/items/1.0392709`.

[35] P. Seppecher, Moving contact lines in the Cahn-Hilliard theory, Int. J. Engng. Sci. 34, 977-992 (1996).

[36] D. Jacqmin, Contact-line dynamics of a diffuse fluid interface, J. Fluid Mech. 402, 57-88 (2000).

[37] T. Qian, X. P. Wang, P. Sheng, Molecular hydrodynamics of the moving contact line in two-phase immiscible flows, Commun. Comput. Phys. 1, 1-52 (2006).

[38] P. Yue, C. Zhou, J. J. Feng, Sharp-interface limit of the Cahn-Hilliard model for moving contact lines, J. Fluid Mech. 645, 279-294 (2010).

[39] M. Wörner, Numerical modeling of multiphase flows in microfluidics and micro process engineering: a review of methods and applications, Microfluid Nanofluid 12, 841-886 (2012).

[40] P. G. De Gennes, J. Prost, The Physics of liquid crystals, 2nd Ed. Clarendon, Oxford, 1993.

[41] M. Kleman, O. D. Lavrentovich, Soft Matter Physics: An Introduction, Springer, New York, 2003.

[42] M. Ravnik, S. Žumer, Landau-de-Gennes modeling of nematic liquid crystal colloids, Liq. Cryst. 36, 1201-1214 (2009).

[43] D. Jacqmin, Calculation of two-phase Navier–Stokes flows using phase-field modeling, J. Comput. Phys. 155, 96-127 (1999).

[44] P. Yue, J. J. Feng, C. Liu, J. Shen, A diffuse-interface method for simulating two-phase flows of complex fluids, J. Fluid Mech. 515, 293-317 (2004).

[45] P. Yue, C. Zhou, J. J. Feng, C. F. Ollivier-Gooch, H. H. Hu, Phase-field simulations of interfacial dynamics in viscoelastic fluids using finite elements with adaptive meshing, J. Comput. Phys. 219, 47-67 (2006).

[46] A. N. Beris, B. J. Edwards, Thermodynamics of flowing systems with internal microstructure, (Oxford University Press, New York, 1994).

[47] C. Denniston, E. Orlandini, J. M. Yeomans, Lattice Boltzmann simulations of liquid crystal hydrodynamics, Phys. Rev. E 63, 056702-1–10 (2001).

[48] J.-C. Loudet, M. Qiu, J. Hemauer, J. J. Feng, Drag force on a particle straddling a fluid interface: Influence of interfacial deformations, Eur. Phys. J. E 43, 13 (2020).

[49] R. M. W. van Bijnen, R. H. J. Otten, P. van der Schoot, Texture and shape of two-dimensional domains of nematic liquid crystals, Phys. Rev. E 86, 051703-1–12 (2012).

[50] S. V. Lishchuk, C. M. Care, I. Halliday, A lattice Boltzmann scheme for a nematic–isotropic interface, J. Phys.: Condens. Matter 16, S1931-S1944 (2004).

[51] COMSOL Multiphysics® v. 5.4 reference manual. See `https://www.comsol.com/documentation`. COMSOL AB, Stockholm, Sweden.

[52] Eq. (12) implies that the interfacial deformations (Δy_I) diverge with the box size L, which is one of the characteristic length scales of the problem in the simple model of Fig. 11 (appendix B). But in more realistic situations, we should rather consider that L is about a few times the particle radius (R), say $\sim 10R$, so that interfacial distortions remain finite of course. This statement is justified by theoretical predictions, which show that the menicus deformation around a colloidal particle floating

at the Iso-N interface is a rapidly decaying function of the distance to the particle (r) (see, e.g., Eq. (11) in [32]). Thus, at $r \sim 10R$, we expect the interfacial distortions to be negligible. A similar treatment applies to the elastic free energy [cf. Eq. (B.1)], which cannot grow indefinitely with L. Taking $L \sim 10R$ as a cut-off distance also agrees with the fact that elastic deformations are a fast decreasing function of the distance to the perturbation (see, e.g., [1]). These considerations do not impact the scaling of Δy_I with w^* and hence the data analysis of Fig. 3.

[53] K. D. Danov, R. Dimova, B. Pouligny, Viscous drag of a solid sphere straddling a spherical or flat interface, Physics of Fluids 12, 2711-2722 (2000).

[54] T. Araki, H. Tanaka, Surface-sensitive particle selection by driving particles in a nematic solvent, J. Phys.: Condens. Matter 18, L193-L203 (2006).

[55] S. Khullar, C. Zhou, J. J. Feng, Dynamic Evolution of Topological Defects around Drops and Bubbles Rising in a Nematic Liquid Crystal, Phys. Rev. Lett. 99, 237802-1–4 (2007).

[56] C. Zhou, P. Yue, J. J. Feng, The rise of Newtonian drops in a nematic liquid crystal, J. Fluid Mech. 593, 385-404 (2007).

[57] D. Reyes-Arango, J. Quintana-H, J. C. Armas-Pérez, H. Híjar, Defects around nanocolloids in nematic solvents simulated by Multi-particle Collision Dynamics, Physica A 547, 123862-1–18 (2020).

[58] A. D. Rey, Marangoni flow in liquid crystal interfaces, J. Chem. Phys. 110, 9769-9770 (1999).

[59] H. Stark, D. Ventzki, Non-linear Stokes drag of spherical particles in a nematic solvent, Europhys. Lett. 57, 60-66 (2002).

[60] J.-W. Kim, H. Kim, M. Lee, J. J. Magda, Interfacial Tension of a Nematic Liquid Crystal/Water Interface with Homeotropic Surface Alignment, Langmuir 20, 8110-8113 (2004).

[61] F. R. Hung, O. Guzmán, B. T. Gettelfinger, N. L. Abbott, J. J. de Pablo, Anisotropic nanoparticles immersed in a nematic liquid crystal: Defect structures and potentials of mean force, Phys. Rev. E 74, 011711-1–12 (2006).